





Strain-induced shape anisotropy in antiferromagnetic structures

Hendrik Meer,^{1,*} Olena Gomonay¹,,¹ Christin Schmitt,¹ Rafael Ramos,^{2,3} Leo Schnitzspan,¹ Florian Kronast,⁴ Mohamad-Assaad Mawass^{1,4},,⁴ Sergio Valencia,⁴ Eiji Saitoh,^{2,5,6,7} Jairo Sinova,^{1,8} Lorenzo Baldrati¹,,¹ and Mathias Kläui^{1,9,†}

¹*Institute of Physics, Johannes Gutenberg-University Mainz, 55099 Mainz, Germany*

²*WPI-Advanced Institute for Materials Research, Tohoku University, Sendai 980-8577, Japan*

³*Centro de Investigación en Química Biológica e Materiais Moleculares (CIQUS),*

Departamento de Química-Física, Universidad de Santiago de Compostela, Santiago de Compostela 15782, Spain

⁴*Helmholtz-Zentrum Berlin für Materialien und Energie, Albert-Einstein-Strasse 15, 12489 Berlin, Germany*

⁵*Department of Applied Physics, The University of Tokyo, Tokyo 113-8656, Japan*

⁶*Center for Spintronics Research Network, Tohoku University, Sendai 980-8577, Japan*

⁷*Advanced Science Research Center, Japan Atomic Energy Agency, Tokai 319-1195, Japan*

⁸*Institut of Physics, Academy of Sciences of the Czech Republic, Praha 11720, Czech Republic*

⁹*Center for Quantum Spintronics, Department of Physics,*

Norwegian University of Science and Technology, 7034 Trondheim, Norway



(Received 25 April 2022; accepted 2 September 2022; published 26 September 2022)

We demonstrate how shape-dependent strain can be used to control antiferromagnetic order in NiO/Pt thin films. For rectangular elements patterned along the easy and hard magnetocrystalline anisotropy axes of our film, we observe different domain structures and we identify magnetoelastic interactions that are distinct for different domain configurations. We reproduce the experimental observations by modeling the magnetoelastic interactions, considering spontaneous strain induced by the domain configuration, as well as elastic strain due to the substrate and the shape of the patterns. This allows us to demonstrate and explain how the variation of the aspect ratio of rectangular elements can be used to control the antiferromagnetic ground-state domain configuration. Shape-dependent strain does not only need to be considered in the design of antiferromagnetic devices, but can potentially be used to tailor their properties, providing an additional handle to control antiferromagnets.

DOI: [10.1103/PhysRevB.106.094430](https://doi.org/10.1103/PhysRevB.106.094430)

Antiferromagnetic materials (AFM) are promising candidates for fast, robust, and energy-efficient spintronic devices [1]. AFMs possess two or more magnetic sublattices, with vanishing net magnetization. This absence of magnetic stray fields enables higher bit packing density of AFM devices compared to ferro(i)magnetic materials (FMs), enhanced robustness against interfering external magnetic fields, and potentially THz switching speeds [2]. Especially insulating antiferromagnetic materials (iAFM) have emerged as a promising material class for the development of low-power devices because their low damping allows for the transport of spin currents over long distances [3].

Crucial for the implementation of AFMs as active spintronic devices is the control of the antiferromagnetic order. In recent years it has been established that current pulses through an adjacent heavy-metal layer can induce a reorientation of the antiferromagnetic ordering in insulating AFMs [4–6]. For iAFMs with strong magnetostriction, the reorientation of the Néel vector is dominated by a thermomagnetoelastic switching and strongly depends on the device geometry [7–9].

For FMs the device geometry and shape-induced control of the domains is a key tool for tailoring functional device

properties. In AFMs, conventional shape anisotropy caused by the magnetic dipolar interactions is not present, due to the absence of a demagnetization field. However, theoretical work on shape-induced phenomena in finite-size antiferromagnets predicts an ordering of the antiferromagnetic domains, with long-range strain fields leading to the formation of shape-dependent domain structures [10,11]. It has been shown that the shape-induced domains in the FM layer of a AFM/FM bilayer can for instance be used to imprint an AFM vortex state into the adjacent AFM layer [12,13]. However, initial studies of patterning-induced effects in antiferromagnetic LaFeO₃ could not observe any changes in the domain structure, after patterning different elements with etching [14]. Later studies patterned elements via an Ar⁺ ion implantation-based patterning technique, which resulted in antiferromagnetic structures embedded in a nonmagnetic layer [15,16]. This technique led to the observation of changes in the antiferromagnetic ordering near the patterning edge for LaFeO₃ [15,17,18] and more recently La_{0.7}Sr_{0.3}FeO₃ [16], interpreted as an edge effect near the edge for elements patterned along the easy axis. Further studies have suggested the exploitation of this effect in exchange-bias applications of AFM and FM heterostructures [19]. However, these previous investigations of patterning-induced modulations of the AFM order have been focused on the passive application of AFMs in bilayers of an AFM and a FM. Considering the potential of antiferromag-

*meer@uni-mainz.de

†Klaeui@Uni-Mainz.de

nets as active elements in spintronic devices, it is important to investigate patterning- and shape-induced effects and, in particular, the control of the domain configuration in AFMs without an adjacent FM layer. It is crucial to not only understand patterning-induced effects near the edge, but also the influence of shape-dependent strain on the domain structure inside a structured antiferromagnetic device. This effect would be most suitable to tailor domain configurations by the shape.

The prototypical collinear antiferromagnet NiO has been considered to be a promising candidate for an active element in spintronic applications, in contrast to LaFeO_3 , due to the possibility of electrically controlling and reading the AFM order [4,20–22] and recent observations of ultrafast currents in the THz regime in NiO/Pt bilayers [2,23]. In addition, NiO exhibits a high Néel temperature of 523 K in the bulk [24] and strong magnetoelastic coupling [25]. The latter has been used extensively to manipulate the AFM order of NiO by growth-induced strain [26–28], piezoelectric substrates exerting strain [29], and indirectly via current-induced heating leading to strain [9]. However, the effect of shape-dependent strain on the domain structure of NiO thin films has not been explored. Considering the application of AFMs with strong magnetostriction like NiO or CoO in active spintronic devices, it is important to investigate how the geometry influences the antiferromagnetic domain configuration and how one could use different geometries to control the antiferromagnetic order.

In this work, we demonstrate the tailoring of the AFM ground-state domain configuration of NiO by shape-dependent strain. We study the Néel vector orientation in patterned elements by photoemission electron microscopy (PEEM) exploiting the x-ray magnetic linear dichroism (XMLD) effect for magnetic contrast. We first identify and compare the shape-induced domain structure of elements oriented along different axes before we theoretically explore how shape-induced effects can manipulate the antiferromagnetic ordering in different element geometries. Finally, we demonstrate how the modification of the shape-dependent strain by variation of the aspect ratio of our elements can be used to control the antiferromagnetic domain configuration, demonstrating thus a tool for the shape-induced control of future AFM devices.

I. RESULTS

To investigate shape-induced effects on the antiferromagnetic domain structure, we have grown an epitaxial NiO(10 nm)/Pt(2 nm) bilayer on an MgO(001) substrate and used Ar ion beam etching to pattern various elements with different orientations. Similarly prepared bilayers of NiO and Pt are currently extensively used for current-induced switching [4–9] and THz radiation experiments [30]. As depicted in Fig. 1(a), we have etched trenches with a width of around $1 \mu\text{m}$ and a depth of about 20 nm around the desired elements. Additionally, we deposited about 1.4 nm of ruthenium inside the trenches to reduce the possibility of discharges during PEEM imaging [31]. To allow for a re-configuration of the AFM domains, the sample was annealed after patterning above its Néel temperature for 10 min at

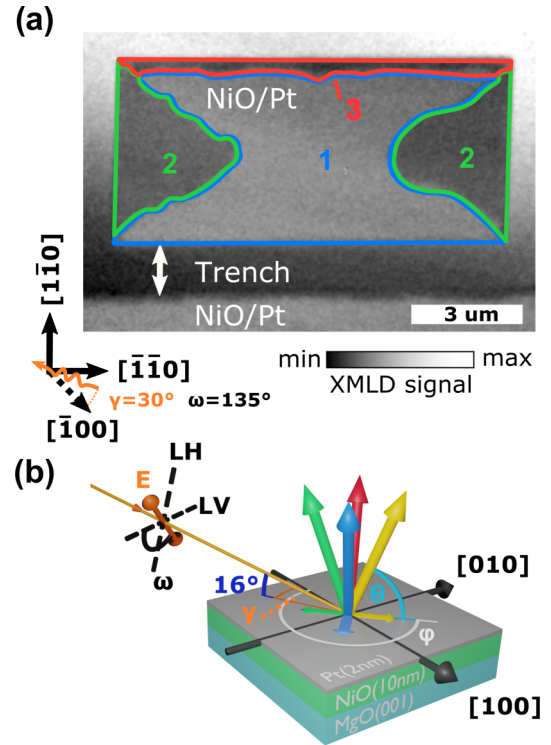


FIG. 1. (a) XMLD-PEEM image of shape-induced NiO domains inside a rectangular-shaped element, with its edges oriented along the in-plane projection of the easy axis. (b) Sketch of the experimental setup and orientation of the observed different Néel vector directions $[\pm 5 \pm 5 19]$ with respect to the polarization vector. An orientation along $[5 5 19]$ (yellow) is equally possible, but was not observed in this particular element.

550 K under vacuum. Measurements were carried out at the UE49-PGM/SPEEM at the BESSY II electron storage ring operated by the Helmholtz-Zentrum Berlin für Materialien und Energie [32].

We first measured polarization-dependent absorption spectra around the Ni L_3 and L_2 edges (details of the measurement technique, see Appendix B) to verify the antiferromagnetic order of our films at room temperature. The XMLD contrast is proportional to the orientation of the Néel vector. By studying the XMLD contrast dependence on the azimuthal angle γ and angle of the beam polarization ω (Appendix B) we can identify in Fig. 1(a) four antiferromagnetic domains present in a rectangular element of $10 \mu\text{m} \times 5 \mu\text{m}$ whose long axis is oriented along the $[110]$ direction. Three different levels of XMLD contrast are observed inside our element, indicating three types of domains, a larger domain in the center (domain 1, blue), two originating from the short edges (domain 2, green), and one narrow at the long edge (domain 3, red). The directions of the Néel vector in the different domains are depicted in Fig. 1(b). We can observe that the in-plane projection of the Néel vector in all domains is oriented orthogonal to the edges of the element along $[110]$ and $[\bar{1}\bar{1}0]$. The formation of domain 3 (red) along the edge can be attributed to localized changes of the anisotropy near the edge of the element, related to patterning-induced material property changes. However, the shape of domains 2 (green)

and 1 (blue) in the center of the element can not be understood by local changes of the anisotropy at the edge of the element and we need to model long-range magnetoelastic interactions to understand the domain configuration.

NiO is known for its strong magnetoelastic coupling which is responsible for the creation of internal (magnetoelastic) stresses in a magnetically ordered state. In a free-standing homogeneously magnetically ordered sample, these stresses induce a pronounced spontaneous strain ($u_0 \propto 10^{-4} - 3 \times 10^{-3}$ [33]) characterized by the strain tensor \hat{u}_0^{spon} whose components are related to the components of the Néel vector \mathbf{n} . In a multilayer system the internal magnetoelastic stresses are complemented by the external stresses due to the clamping of the antiferromagnetic layer by a nonmagnetic substrate [34]. In this case the resulting strain field can be split into two parts, spontaneous (or plastic) strains $\hat{u}_0^{\text{spon}}[\mathbf{n}(\mathbf{r})]$ associated with the distribution of the Néel vector (as in the absence of a substrate) and additional, elastic strains \hat{u}^{elast} : $\hat{u}^{\text{tot}} = \hat{u}_0^{\text{spon}} + \hat{u}^{\text{elast}}$.

To calculate the elastic strain, we use an approach of elasticity theory with continuously distributed defects [35,36]. In particular, we assume that in magnetic multilayers the defects originate from the incompatibility between the spontaneous strain \hat{u}_0^{spon} and the nondeformed (reference) state of a nonmagnetic substrate at the NiO/substrate interface, or from incompatibility between spontaneous strain in neighboring domains. From the compatibility condition for the total strain $\varepsilon_{ijk}\varepsilon_{lmn}\partial_j\partial_m u_{kn}^{\text{tot}} = 0$ (where ε_{ijk} is an antisymmetric Levi-Civita tensor) we obtain a set of equations for the elastic strains

$$\varepsilon_{ijk}\varepsilon_{lmn}\partial_j\partial_m u_{kn}^{\text{elast}} = \eta_{il}, \quad (1)$$

in which the incompatibility tensor $\eta_{il} \equiv -\varepsilon_{ijk}\varepsilon_{lmn}\partial_j\partial_m u_{kn}^{\text{spon}}[\mathbf{n}(\mathbf{r})]$ is calculated for a given distribution of the Néel vector.

Equation (1) is similar to equations of electrostatics, in which the incompatibility $\hat{\eta}$ plays the role of the elastic or magnetoelastic charges and the elastic strains \hat{u}^{elast} correspond to the potentials [37]. Moreover, similar to the electric and magnetostatic stray fields, the field of the corresponding elastic strains is long range and therefore can stabilize an inhomogeneous distribution of the magnetic vectors. The similarity with the equations of electrostatics and magnetostatics allows for a qualitative interpretation of the magnetoelastic effects in terms of magnetoelastic charge distributions.

Here, we consider some of the effects that reinforce our intuitive reasoning through modeling. The theoretical description of magnetic textures is based on minimizing the total energy of a sample with respect to magnetic and elastic variables. The bulk energy of the NiO film,

$$W_{\text{bulk}} = \int d\mathbf{r}(w_{\text{mag}} + w_{\text{me}} + w_{\text{elas}}), \quad (2)$$

includes magnetic w_{mag} , magnetoelastic w_{me} , and elastic w_{elas} contributions. The magnetic structure of NiO is described by the Néel vector $\mathbf{n}(\mathbf{r})$ ($|\mathbf{n}| = 1$), which is generally parametrized with two angles, φ and ϑ , as shown in Fig. 1(b).

We distinguish in our thin NiO films four types of T domains with the Néel vector oriented along $[\pm 5 \pm 5 19]$ [38]. The pairs with opposite orientation of projection on the film plane have the same in-plane components of spontaneous

strain and will be treated in the further discussion as the same domain. Since the out-of-plane component of the Néel vector is the same in all domains, we consider the in-plane angle φ as the only magnetic variable. We also neglect the magnetic homogeneity throughout the thickness of the NiO layer and consider the distribution of the Néel vector to be within the film plane (xy).

We start with a discussion of the origin of the domain structure in thin films and patterned elements. A single-domain continuous film of NiO is charged due to incompatibility strain charges homogeneously distributed at the interface with the nonmagnetic substrate. The charge density depends on the elastic and magnetoelastic properties of the interface and is localized in a thin layer of the order of the exchange length (characteristic length scale at which the Néel vector decays inside the nonmagnetic region) (see Appendix C). These magnetoelastic charges create additional homogeneous strain \hat{u}^{elast} and their non-negative contribution to the energy of the NiO layer is proportional to the volume of the NiO.

In a multidomain sample with equally distributed domains of all types, the average strain incompatibility and average charge density vanish. The local charge density is still nonzero and contributes to the energy of the sample. However, this contribution is proportional to the average domain volume. Hence, a small-scale multidomain structure is energetically favorable, with the domain size being limited by the positive-energy contribution of the domain walls (similar to the Kittel model in ferromagnets [39]). However, the formation of a new domain inside a single-domain region is blocked by a high-energy barrier associated with the coherent rotation of a large number of magnetic moments in the two sublattices. The energy barrier can be much lower at the sample surfaces and edges due to the additional contributions from surface energy and incompatibility charges at the element corners [34].

First, we consider the role of the surface magnetic anisotropy present in thin-film NiO continuous films and patterned elements, which in our case favors alignment of the Néel vector perpendicular to the surface. For this we studied the evolution of the magnetic structure in the patterned elements with different aspect ratio cut parallel to the in-plane projection of the magnetic easy axis [see Fig. 2(a)].

In this geometry the surface anisotropy induces the formation of the dark domains along $[\bar{1}10]$ edges and bright domains along $[110]$ edges. The final texture includes two closure domains localized at the short edges and a large orthogonal domain that spreads between the two long edges. The closure domains grow from the edges due to magnetoelastic forces that act to diminish the average magnetoelastic charge of the sample. This growth is limited by an increase of the energy of the domain walls. The size of the closure domains is of the order of the size of the short edge and depends on the aspect ratio of the sample [see Fig. 2(b)]. It should be noted that in the absence of magnetoelastic coupling, the closure domains would be localized in the vicinity of the short edge within a distance of several magnetic domain wall widths (Fig. 3), independent on the aspect ratio of the device. Our simulations also show that the closure domains can be localized along the longer edges of the samples as well, as could be experimentally observed for larger patterned devices. However, both configurations (the one with the closure domains along the

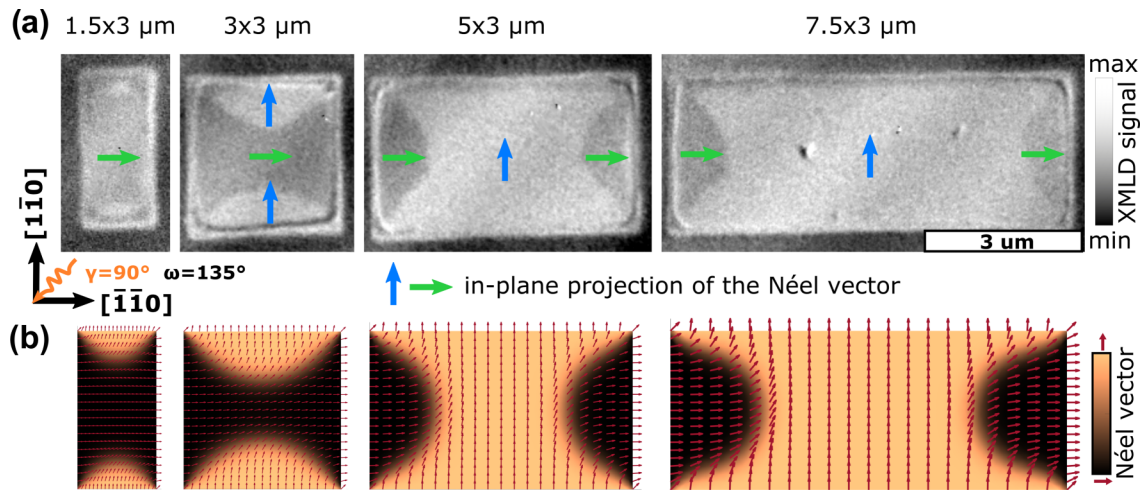


FIG. 2. (a) XMLD images of different NiO(10)/Pt(2) rectangular devices with varying aspect ratio. The edges of the devices are oriented along the in-plane projection of the easy axes. The arrows show the in-plane projection of the Néel vector determined from the grayscale contrast. (b) Final equilibrium state of the magnetic texture after considering magnetoelastic interactions to simulate the domain distribution in different aspect ratios. The color code indicates the direction of the Néel vector.

short and the other along the long edges) are observed in a finite range of aspect ratios (between $\frac{1}{3}$ and 3) for which their energies have comparable values. In this case the structure of the final state depends on the initial configuration and kinetics of the domain growth.

To better illustrate the effect of strain, we next investigate elements oriented along the [100] and [010] axes, where even more conspicuous effects are expected. For elements oriented along the projection of the hard axes the domains do not align along the edges of the element, but instead are centered around the corners of the elements [see Fig. 4(a)]. Inside the element we can observe a large green domain and two blue domains, which are located near the top left and bottom right corner. Outside of the element we observe a domain (green

arrows) and two additional domains (blue arrows) located at the top right and bottom left corner, opposite to the domains in the inner corners. In the case that the domain formation is dominated by an alignment along certain crystallographic axes one would expect the same domains to be present at the inside and outside edges of the element. However, this is not the case and we therefore need to consider shape-dependent strain, in particular the role of incompatibility charges in the corners of the elements, to understand the origin of the domain structure.

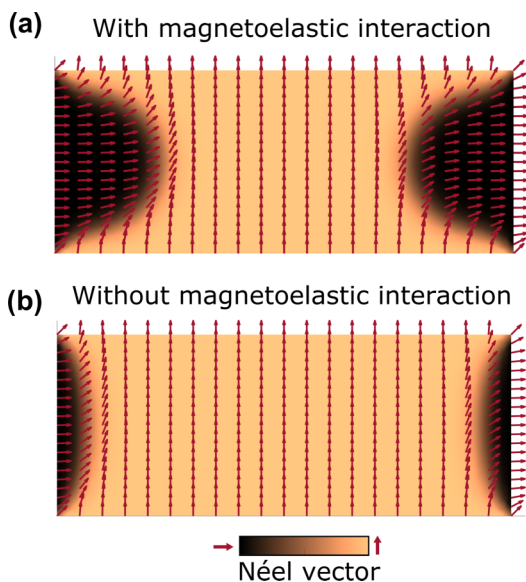


FIG. 3. Comparison between equilibrium states with (a) and without (b) consideration of magnetoelastic coupling.

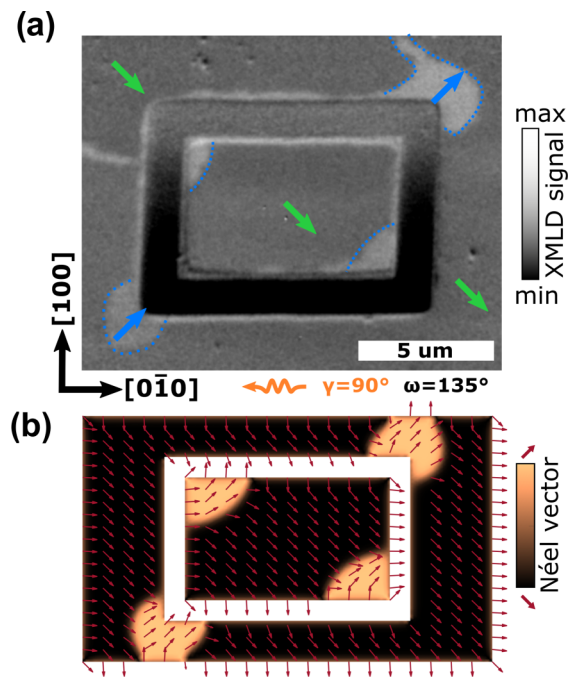


FIG. 4. (a) Antiferromagnetic domain structure of a rectangular-shaped element oriented along the in-plane projections of the hard axes. (b) Simulated equilibrium state of the magnetic texture. The color code and the arrows indicate the direction of the Néel vector.

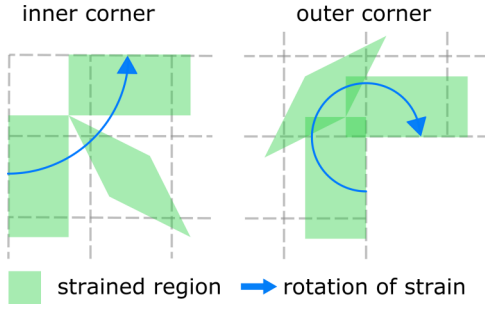


FIG. 5. Sketch of the different direction of the rotation for strain at inner and outer corners.

For elements cut along the in-plane projection of the magnetic hard axis, the surface anisotropy favors an orientation of the Néel vector along a hard magnetic axis and does not set a preferable domain type. However, the surface anisotropy sets orthogonal easy directions at neighboring edges and favors the formation of vortexlike textures of the Néel vectors in the vicinity of the sample corners. Such a rotation of the Néel vector through 90° is associated with an inhomogeneous rotation of the spontaneous strain \hat{u}_0^{spont} and creates an elastic vortex structure, so-called disclinations [36,40], localized in the corners. Each disclination is characterized by incompatibility charges which have opposite sign in neighboring corners (see Fig. 5). These charges create a radially distributed field of elastic strain \hat{u}^{elast} [36] that via magnetoelastic coupling sets preferable directions for the Néel vector along the bisectrices of the element. For the elements cut along the magnetic easy axis, this strain couples with the orientation of the Néel vector in the center of the domain walls and splits the energy of the domain walls pinned to the neighboring corners. For the elements cut along the magnetic hard axis it removes the degeneracy between the bright and dark domains and facilitates a formation of the domain of a certain type. In other words, the elastic strains lower the energy barrier for a closure domain. Here, the closure domain starts to grow from the opposite corners, which have the same sign of rotation, as shown in Fig. 4(b). Interestingly, such magnetoelastic disclinations appear not only at the inner corners of the rectangular elements, but also at the corners of the outer part of the element, where the spontaneous strain rotates in the opposite direction [41].

Hence, internal and external strain charges of the same corner have opposite signs. As a result, the closure domains of the same type start to grow along the different diagonals in the internal and external regions [see Figs. 4(a) and 4(b)]. Magnetoelastic disclinations (corner charges) are present also in the elements cut along the magnetic easy axes. In this case, corresponding elastic strains set a preferable direction of the Néel vector inside the domain walls near the corners. Our calculations show a difference of domain wall width and pinning energy in the neighboring corner as a result of the strain-induced anisotropy.

In addition, different antiferromagnetic domains are accompanied by the deformation of the crystallographic structure. Due to the need for mechanical equilibrium, the creation of antiferromagnetic domains is accompanied by destressing effects [10,42]. The total energy of a patterned element is

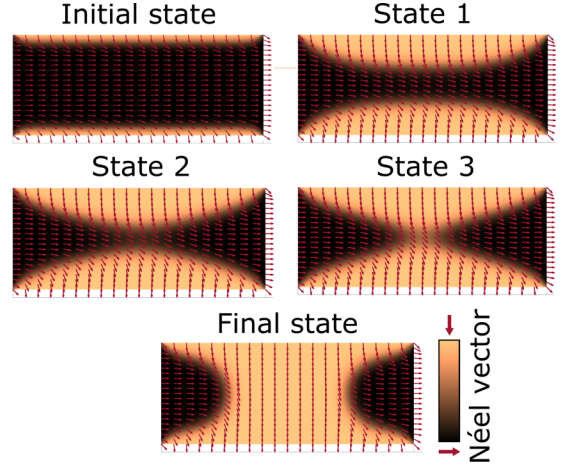


FIG. 6. Simulated evolution of the domain structure from the initial state to the final equilibrium state.

here complemented by the destressing energy W_{destr} , which describes the coupling with the nonmagnetic substrate and edge effects, and the surface energy W_{surf} of the patterned edges. The surface energy is modeled in a way to favor an orientation of the Néel vector parallel to the normal \mathbf{N} with respect to the patterned edge:

$$W_{\text{surf}} = -K_{\text{surf}} \oint (\mathbf{n} \cdot \mathbf{N})^2 d\ell. \quad (3)$$

Here, the constant $K_{\text{surf}} > 0$ parametrizes the surface energy and ℓ is the coordinate along the sample edge. The destressing energy, W_{destr} , is treated as an additional contribution of the elastic strains \hat{u}^{elast} , which maintains the strain compatibility of the sample at the interface with nonmagnetic substrate.

To demonstrate the role of incompatibility and the destressing effects in the formation and stabilization of the domain structure, we have calculated the evolution of the domain structure for elements along the in-plane projection of the easy axes, starting from the almost homogeneous state (domain 2, green) with small domains (domain 1, blue) localized at the long edges of the sample using different values of the damping parameter (different rates of the energy losses). At the initial stage, the closure domains (at the long edge), being pinned in the corners, grow in size trying to reduce the average incompatibility of the sample (see Fig. 6). In case of slow (quasistatic) relaxation (large damping) the system evolves into a state with the closure domains 1 along the long edges separated by domain 2. In the opposite case of small damping, the closure domains merge and the final state corresponds to the closure domains of the type 2 localized at the short edges.

II. DISCUSSION

By investigating elements with different orientations and aspect ratios etched into NiO/Pt bilayers, we identify long-range strain to govern the shape-dependent formation of antiferromagnetic domains. We observe a preferential orientation of the Néel vector perpendicular to the edge of our devices due to patterning effects. Consistent with our previous observations the lattice mismatch between the MgO substrate

and the NiO layer leads to a stabilization of different T domains with the largest out-of-plane components, due the strain in the out-of-plane direction [38]. We investigate the domain structures of elements oriented along the projection of the easy and hard axes and can identify shape-dependent strain to be responsible for the observed domain structures. We can reproduce our experimental observations by magnetoelastic modeling that accounts for the spontaneous strain, due to the distribution of the Néel vector, and elastic strain due to contributions from the substrate and the patterning. In previous studies, the substrate-induced strain is the same for the different T domains [38]. Here, however, the shear strain due to the domain formation varies for the different domains across the different geometries. The strain that dominates the formation of the domain structure does not arise from patterning-induced strain, but from the strain that is associated with the formation of each T domain. The interactions between these strains are responsible for the formation and stabilization of the equilibrium domain structure. Analogous to shape anisotropy in ferromagnets, magnetoelastic interactions in antiferromagnets are long range and can be used to tailor the antiferromagnetic ground state of antiferromagnetic devices. For example, by choosing the right size, aspect ratio, and orientation one could use shape-induced strain to control the antiferromagnetic ground state in antiferromagnetic THz emitters to tailor and optimize their response [30]. In addition, the strain from the patterned device itself could be used in electrical switching of antiferromagnets to support or hinder the reorientation of the Néel vector independent of the underlying switching mechanism.

Finally, we note that long-range magnetoelastic interactions in AFMs could also be a challenge for the development of antiferromagnetic data storage as reorienting the Néel order to switch bits will by the change in strain affect neighboring bits. However, by considering physical separation, as in established bit-patterned media [43], the noninteracting nature of AFMs can be fully taken advantage of due to the absence of magnetic stray fields.

In summary, we identify how shape-dependent strain can be used to control the antiferromagnetic ground state in NiO over several microns. Since magnetoelastic coupling is significant for several other antiferromagnets such as CoO and hematite, shape-induced strain can be considered to be the antiferromagnetic equivalent of conventional shape-induced anisotropy in ferromagnets and provides a unique means to control antiferromagnets.

ACKNOWLEDGMENTS

The authors thank T. Reimer for skillful technical assistance. We thank HZB for the allocation of synchrotron radiation beam time, and we thankfully acknowledge the financial support by HZB. The work has benefited from insights gained from experiments that were performed at the CIRCE beamline at ALBA Synchrotron with the collaboration of ALBA staff. L.B. acknowledges the European Union's Horizon 2020 research and innovation program under the Marie Skłodowska-Curie Grant Agreement No. ARTES 793159. L.B. and M.K. acknowledge support from the Graduate School of Excellence Materials Science in Mainz (MAINZ)

Grant No. DFG 266, the DAAD (Spintronics network, Project No. 57334897 and Insulator Spin-Orbitronics, Project No. 57524834), and all groups from Mainz acknowledge that this work was funded by the Deutsche Forschungsgemeinschaft (DFG, German Research Foundation), TRR Grant No. 173-268565370 (Projects No. A01, No. A03, No. A11, No. B02, and No. B12) and KAUST (Grant No. OSR-2019-CRG8-4048). J.S. additionally acknowledges the Alexander von Humboldt Foundation and O.G. and J.S. acknowledge the EU FET Open RIA Grant No. 766566 and the Deutsche Forschungsgemeinschaft (DFG, German Research Foundation), Grant No. TRR 288-422213477 (Project No. A09) and the Grant Agency of the Czech Republic Grant No. 19-28375X. R.R. also acknowledges support from the European Commission through the Project 734187-SPICOLOST (Grant No. H2020-MSCA-RISE-2016), the European Union's Horizon 2020 research and innovation program through the Marie Skłodowska-Curie Actions Grant Agreement No. SPEC 894006, the MCIN/AEI (Grant No. RYC 2019-026915-I), the Xunta de Galicia (Grant No. ED431B 2021/013, Centro Singular de Investigación de Galicia Accreditation 2019-2022, Grant No. ED431G 2019/03), and the European Union [European Regional Development Fund (ERDF)]. M.K. acknowledges financial support from the Horizon 2020 Framework Programme of the European Commission under FET-Open Grant Agreement No. 863155 (s-Nebula) and from the Research Council of Norway through its Centers of Excellence funding scheme, Project No. 262633 "QuSpin." This work was also supported by ERATO "Spin Quantum Rectification Project" (Grant No. JPMJER1402) and the Grant-in-Aid for Scientific Research on Innovative Area, "Nano Spin Conversion Science" (Grant No. JP26103005), Grant-in-Aid for Scientific Research (S) (Grant No. JP19H05600) from JSPS KAKENHI, Japan.

APPENDIX A: SAMPLE PREPARATION

Similar to previous studies [6,38] we used reactive magnetron sputtering to grow epitaxial MgO(001)/NiO(10nm)/Pt(2 nm) thin films. Before deposition the MgO(001) substrates were preannealed at 770° for 2 h in vacuum. We then deposited NiO from a Ni target at 430 °C and 150 W in an atmosphere of O₂ (flow 3 sccm) and Ar (flow 15 sccm), before depositing the platinum layer *in situ* at room temperature.

APPENDIX B: XMLD SIGNAL

We observed x-ray magnetic linear dichroism (XMLD) in Fig. 7(a), calculated as $I_{LH}-I_{LV}$, and an absence of circular magnetic dichroism (XMCD) in Fig. 7(b), indicating purely antiferromagnetic ordering of our films. For subsequent XMLD imaging we utilized the inversion of the XMLD contrast at the Ni L_2 edge at the energies $E_1 = 868.3$ eV, $E_2 = 870.1$ eV and calculated the XMLD image by $[I(E_1)-I(E_2)]/[I(E_1)+I(E_2)]$. By studying the XMLD contrast dependence on the azimuthal angle γ and angle of the beam polarization ω we can identify in Fig. 1(a) four different antiferromagnetic domains to be present in a rectangular element

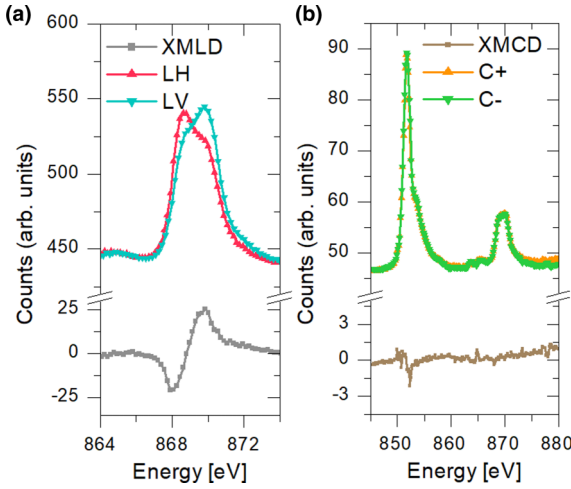


FIG. 7. (a) X-ray absorption spectrum and XMLD for linear polarized x rays in the vicinity of the L_2 edge. (b) X-ray absorption spectrum and XMCD for circular polarized x rays.

of $10 \times 5 \mu\text{m}$ whose long axis is oriented along the $[110]$ direction.

NiO is a compensated collinear antiferromagnet with two magnetic sublattices whose magnetic structure is uniquely described by the Néel vector \mathbf{n} . In bulk NiO crystals the exchange striction leads to a rhombohedral contraction along the $\langle 111 \rangle$ axes. Thus, four twin T domains can be formed with the spins being ferromagnetically coupled inside the $\{111\}$ planes and antiferromagnetically between the $\{111\}$ planes, due to the superexchange interaction. Within such a T domain the spins can be oriented along three possible easy axes $\langle 11\bar{2} \rangle$, leading to three different spin domains S domains per T domain. There are a total of 12 possible domains in bulk NiO crystals [24,44,45]. However, in NiO thin films the growth-induced strain from the substrate mismatch can lead to a preferential stabilization of S domains parallel or perpendicular to the sample plane [27,28]. In a previous study on similarly grown MgO/NiO(10)/Pt(2) thin films we observed that the epitaxial growth of NiO on MgO substrates results in compressive strain, which led to a preferential out-of-plane component of the Néel vector [27,28,38]. Here, we have observed analogous contrast changes among the domains with varying azimuthal angle γ and orientation of the linear beam polarization ω in Fig. 8. Thus, we can identify the orientation of the Néel vector of our domains to be along the $[\pm 5 \pm 5 19]$ directions, in line with our previous findings [38].

APPENDIX C: MODELING OF THE MAGNETIC TEXTURES

We model these contributions according to the tetragonal crystallographic symmetry of the NiO film (deformed cubic crystal due to the substrate), so that the density of the magnetic energy is given by

$$w_{\text{mag}} = \frac{1}{2}A(\nabla\varphi)^2 - \frac{1}{4}H_{\text{an}}M_s \cos 4\varphi, \quad (\text{C1})$$

where A is the exchange stiffness of NiO, H_{an} is the anisotropy field, and $M_s/2$ is the saturation magnetization of the magnetic sublattice. The densities of magnetoelastic and elastic energy

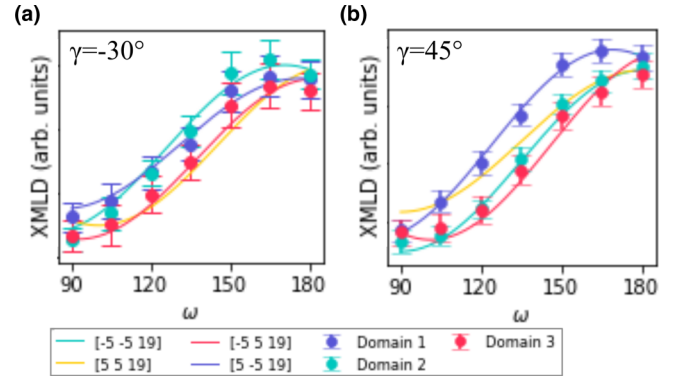


FIG. 8. Simulated and experimental contrast of the different domains dependent on the beam polarization for (a) $\gamma = -30^\circ$ and (b) $\gamma = 45^\circ$.

are

$$w_{\text{me}} = \lambda_{\text{me}}M_s^2[\cos 2\varphi(u_{xx} - u_{yy}) + 2 \sin 2\varphi u_{xy}],$$

$$w_{\text{elas}} = \frac{1}{2}\mu[(u_{xx} - u_{yy})^2 + 4u_{xy}^2] + \frac{\mu}{2(1-2\nu)}(u_{xx} + u_{yy})^2, \quad (\text{C2})$$

where λ_{me} is the magnetoelastic parameter, μ is the shear modulus, ν is the Poisson ratio. In Eq. (C2), we omit the out-of plane components of strain (u_{zz} , u_{xz} , u_{yz}) and disregard the coupling between the Néel vector and the isotropic strain ($u_{xx} + u_{yy}$) since these effects are irrelevant for the formation of the domain structure. The coordinate axes x and y are aligned along the magnetic easy axes $[1\bar{1}0]$ and $[110]$. General expressions for these contributions can be found in [38,46].

The strain in the NiO layer is represented as a sum of spontaneous (plastic) strains and elastic strains, as described in the main part: $\hat{u}^{\text{tot}} = \hat{u}_0^{\text{spon}} + \hat{u}^{\text{elast}}$. The spontaneous strains are calculated by minimizing the elastic and magnetoelastic energy contributions (C2) for a given value of $\varphi(x, y)$:

$$u_{xx}^{\text{spon}} = -u_{yy}^{\text{spon}} = -\frac{\lambda_{\text{me}}}{\mu}M_s^2 \cos 2\varphi,$$

$$u_{xy}^{\text{spon}} = -\frac{\lambda_{\text{me}}}{\mu}M_s^2 \sin 2\varphi. \quad (\text{C3})$$

The elastic strains \hat{u}^{elast} are then calculated from the compatibility equations

$$\varepsilon_{ijk}\varepsilon_{lmn}\partial_j\partial_m u_{kn}^{\text{elast}} = \eta_{il}, \quad (\text{C4})$$

The incompatibility arising at the interface between the magnetic and the nonmagnetic layer is calculated as

$$\eta_{xx} = -\eta_{yy} = \frac{\lambda_{\text{me}}}{\mu}(\partial_z M_s)^2 \cos 2\varphi,$$

$$\eta_{xy} = \frac{\lambda_{\text{me}}}{\mu}(\partial_z M_s)^2 \sin 2\varphi. \quad (\text{C5})$$

The magnetic order, parametrized as $M_s(z)$, vanishes at the scale of the exchange length ξ_{exch} (\propto several interatomic distances), which is much smaller than the other length scales in the system (domain wall width, thickness of the NiO layer, etc.). We can assume that the incompatibility charges (C5)

are localized at the interface $z = 0$ and substitute $(\partial_z M_s)^2 \Rightarrow M_s^2 \delta(z)/\xi_{\text{exch}}$. For the elastic strains \hat{u}^{elas} that are created by incompatibility charges (C5), we use the Eshelby solution [37], so that

$$\begin{aligned} u_{xx}^{\text{elas}}(\mathbf{r}) &= -u_{yy}^{\text{elas}}(\mathbf{r}) = \frac{u_0}{4\pi} \int d\mathbf{r}' \frac{\cos 2\varphi(\mathbf{r}')}{|\mathbf{r} - \mathbf{r}'|}, \\ u_{xy}^{\text{elas}}(\mathbf{r}) &= \frac{u_0}{4\pi} \int d\mathbf{r}' \frac{\sin 2\varphi(\mathbf{r}')}{|\mathbf{r} - \mathbf{r}'|}, \end{aligned} \quad (\text{C6})$$

where $u_0 \equiv \lambda_{\text{me}} M_s^2 / \mu$ is the value of the spontaneous strain.

By substituting Eqs. (C6) into Eq. (2) we obtain the expression for the destressing energy as

$$W_{\text{destr}} = \kappa \int d\mathbf{r} \int d\mathbf{r}' \frac{\cos 2[\varphi(\mathbf{r}') - \varphi(\mathbf{r})]}{|\mathbf{r} - \mathbf{r}'|}. \quad (\text{C7})$$

Here, κ is a phenomenological coefficient that generally depends on the elastic properties of both the magnetic and nonmagnetic layers and the interface. In a simplified model with isotropic magnetoelastic and elastic interactions $\kappa \propto \mu u_0^2 / (4\pi)$. We calculate the distribution of the magnetic variable $\varphi(\mathbf{r})$ from the following set of equations, which minimizes the energy of the sample $W_{\text{bulk}} + W_{\text{destr}}$:

$$\begin{aligned} -x_{\text{DW}}^2 \Delta \varphi + \sin 4\varphi &= \frac{2\kappa}{H_{\text{an}} M_s} \int d\mathbf{r}' \frac{\sin 2[\varphi(\mathbf{r}') - \varphi(\mathbf{r})]}{|\mathbf{r} - \mathbf{r}'|} \\ &+ \frac{2\lambda_{\text{me}} M_s}{H_{\text{an}}} [(u_{xx} - u_{yy}) \sin 2\varphi \\ &- 2u_{xy} \cos 2\varphi], \\ \Delta \mathbf{u} + \frac{1}{1 - 2\nu} \nabla(\nabla \cdot \mathbf{u}) &= 2u_0 \begin{pmatrix} \partial_x(\cos 2\varphi) + \partial_y(\sin 2\varphi) \\ \partial_x(\sin 2\varphi) - \partial_y(\cos 2\varphi) \end{pmatrix}, \end{aligned} \quad (\text{C8})$$

where $x_{\text{DW}} \equiv \sqrt{A/H_{\text{an}} M_s}$ is the domain wall width, and \mathbf{u} is the displacement vector. The second and third equations correspond to conditions of mechanical equilibrium (zero stresses) inside the NiO layer.

Equations (C8) are complemented by the boundary conditions at the edges:

$$\begin{aligned} -\mathbf{AN} \cdot \nabla \varphi + K_{\text{surf}} [(N_x^2 - N_y^2) \sin 2\varphi + 2N_x N_y \cos 2\varphi] &= 0, \\ -\mathbf{N} \cdot \nabla \mathbf{u} + 2u_0 \begin{pmatrix} N_x \cos 2\varphi + N_y \sin 2\varphi \\ N_x \sin 2\varphi - N_y \cos 2\varphi \end{pmatrix} &= 0. \end{aligned} \quad (\text{C9})$$

While the strain distribution within the film plane can be calculated directly from the elasticity equations (C8), we also introduce an approach based on the associated incompatibility

component

$$\eta_{zz} \equiv -u_0 [(\partial_x^2 - \partial_y^2) \cos 2\varphi - 2\partial_x \partial_y \sin 2\varphi]. \quad (\text{C10})$$

This component is mainly concentrated in the sample corners, where it creates partial disclinations and facilitates the formation of domains. To understand this effect, we consider the immediate vicinity of a corner. Strong surface anisotropy aligns the Néel vector at the edges along \mathbf{N} direction. Inside the sample the Néel vector rotates through 90° to fit the boundary conditions. Due to the magnetoelastic mechanism, such a rotation creates a nonzero lattice curvature, which is described by the components of the bend-twist tensor [36]

$$K_{zx} = -\frac{u_0 Y}{\sqrt{X^2 + Y^2}}, \quad K_{zy} = \frac{u_0 X}{\sqrt{X^2 + Y^2}}, \quad (\text{C11})$$

with the XY coordinate frame centered at the corner. According to Eq. (C10) the associated incompatibility $\eta_{zz} \approx \pm 2u_0 / (X^2 + Y^2)$. The sign of η_{zz} depends on the direction of the rotation and is opposite for the neighboring corners (see Fig. 5).

Such a distribution of lattice curvature and incompatibility charge can be treated as an elastic defect, known as a straight disclination line [47], with the Frank vector (vector of disclination) $\Omega = 2\pi u_0$ pointing along z direction. Similar disclinations of magnetoelastic origin that appear at the junctions of several domain walls in ferromagnets were described by Kleman *et al.* [36]. The elastic strains created by the disclination according to [36] are

$$\begin{aligned} u_{xx}^{\text{elas}} - u_{yy}^{\text{elas}} &= -\frac{u_0}{2(1 - \nu)} \frac{X^2 - Y^2}{X^2 + Y^2}, \\ u_{xy}^{\text{elas}} &= -\frac{u_0}{2(1 - \nu)} \frac{XY}{X^2 + Y^2}. \end{aligned} \quad (\text{C12})$$

The strain component u_{xy}^{elas} , which is maximal along bisectrix $X = Y$, sets the preferable direction of the Néel vector either along or perpendicular to the bisectrix direction, depending on the sign of the incompatibility charge. It should be mentioned that incompatibility charges in the inner and outer corners have opposite signs (due to opposite direction of the rotation), thus favoring the formation of domains of different types.

Numerical simulations of the textures were implemented by solving Eqs. (C8) and (C9) with PDE tools of MATLAB2021 with the following parameters: $x_{\text{DW}} = 100$ nm, $u_0 = 3 \times 10^{-5}$, $H_{\text{an}} = 0.03$ T, $M_s = 10^6$ A/m, $\mu = 35$ GPa. The equilibrium structure was calculated by the relaxation from different initial states with the loops for self-correction of the destressing energy (see Fig. 6). To obtain a multidomain structure, we always introduced a domain wall into the system (either 180° or 90°).

- [1] V. Baltz, A. Manchon, M. Tsoi, T. Moriyama, T. Ono, and Y. Tserkovnyak, *Rev. Mod. Phys.* **90**, 015005 (2018).
- [2] T. Kampfrath, A. Sell, G. Klatt, A. Pashkin, S. Mährlein, T. Dekorsy, M. Wolf, M. Fiebig, A. Leitenstorfer, and R. Huber, *Nat. Photonics* **5**, 31 (2011).
- [3] R. Lebrun, A. Ross, S. A. Bender, A. Qaiumzadeh, L. Baldrati, J. Cramer, A. Brataas, R. A. Duine, and M. Kläui, *Nature (London)* **561**, 222 (2018).

- [4] T. Moriyama, K. Oda, T. Ohkochi, M. Kimata, and T. Ono, *Sci. Rep.* **8**, 14167 (2018).
- [5] X. Z. Chen, R. Zarzuela, J. Zhang, C. Song, X. F. Zhou, G. Y. Shi, F. Li, H. A. Zhou, W. J. Jiang, F. Pan, and Y. Tserkovnyak, *Phys. Rev. Lett.* **120**, 207204 (2018).
- [6] L. Baldrati, O. Gomonay, A. Ross, M. Filianina, R. Lebrun, R. Ramos, C. Leveille, F. Fuhrmann, T. R. Forrest, F. Maccherozzi,

- S. Valencia, F. Kronast, E. Saitoh, J. Sinova, and M. Kläui, *Phys. Rev. Lett.* **123**, 177201 (2019).
- [7] G. P. Zhang, Y. H. Bai, T. Jenkins, and T. F. George, *J. Phys.: Condens. Matter* **30**, 465801 (2018).
- [8] L. Baldrati, C. Schmitt, O. Gomonay, R. Lebrun, R. Ramos, E. Saitoh, J. Sinova, and M. Kläui, *Phys. Rev. Lett.* **125**, 077201 (2020).
- [9] H. Meer, F. Schreiber, C. Schmitt, R. Ramos, E. Saitoh, O. Gomonay, J. Sinova, L. Baldrati, and M. Kläui, *Nano Lett.* **21**, 114 (2021).
- [10] H. V. Gomonay and V. M. Loktev, *Phys. Rev. B* **75**, 174439 (2007).
- [11] O. Gomonay, S. Kondovych, and V. Loktev, *J. Magn. Magn. Mater.* **354**, 125 (2014).
- [12] J. Wu, D. Carlton, J. S. Park, Y. Meng, E. Arenholz, A. Doran, A. T. Young, A. Scholl, C. Hwang, H. W. Zhao, J. Bokor, and Z. Q. Qiu, *Nat. Phys.* **7**, 303 (2011).
- [13] J. Sort, K. S. Buchanan, V. Novosad, A. Hoffmann, G. Salazar-Alvarez, A. Bollero, M. D. Baró, B. Dieny, and J. Nogués, *Phys. Rev. Lett.* **97**, 067201 (2006).
- [14] S. Czekaj, F. Nolting, L. J. Heyderman, K. Kunze, and M. Krüger, *J. Phys.: Condens. Matter* **19**, 386214 (2007).
- [15] E. Folven, T. Tybell, A. Scholl, A. Young, S. T. Retterer, Y. Takamura, and J. K. Grepstad, *Nano Lett.* **10**, 4578 (2010).
- [16] M. S. Lee, P. Lyu, R. V. Chopdekar, A. Scholl, S. T. Retterer, and Y. Takamura, *J. Appl. Phys.* **127**, 203901 (2020).
- [17] E. Folven, A. Scholl, A. Young, S. T. Retterer, J. E. Boschker, T. Tybell, Y. Takamura, and J. K. Grepstad, *Phys. Rev. B* **84**, 220410(R) (2011).
- [18] E. Folven, Y. Takamura, and J. K. Grepstad, *J. Electron Spectrosc. Relat. Phenom.* **185**, 381 (2012).
- [19] E. Folven, J. Linder, O. V. Gomonay, A. Scholl, A. Doran, A. T. Young, S. T. Retterer, V. K. Malik, T. Tybell, Y. Takamura, and J. K. Grepstad, *Phys. Rev. B* **92**, 094421 (2015).
- [20] G. R. Hoogeboom, A. Aqeel, T. Kuschel, T. T. M. Palstra, and B. J. van Wees, *Appl. Phys. Lett.* **111**, 052409 (2017).
- [21] L. Baldrati, A. Ross, T. Niizeki, C. Schneider, R. Ramos, J. Cramer, O. Gomonay, M. Filianina, T. Savchenko, D. Heinze, A. Kleibert, E. Saitoh, J. Sinova, and M. Kläui, *Phys. Rev. B* **98**, 024422 (2018).
- [22] J. Fischer, O. Gomonay, R. Schlitz, K. Ganzhorn, N. Vlietstra, M. Althammer, H. Huebl, M. Opel, R. Gross, S. T. B. Goennenwein, and S. Geprägs, *Phys. Rev. B* **97**, 014417 (2018).
- [23] T. Moriyama, K. Hayashi, K. Yamada, M. Shima, Y. Ohya, and T. Ono, *Phys. Rev. Mater.* **4**, 074402 (2020).
- [24] W. L. Roth, *J. Appl. Phys.* **31**, 2000 (1960).
- [25] E. Aytan, B. Debnath, F. Kargar, Y. Barlas, M. M. Lacerda, J. X. Li, R. K. Lake, J. Shi, and A. A. Balandin, *Appl. Phys. Lett.* **111**, 252402 (2017).
- [26] A. Kozioł-Rachwał, M. Ślęzak, M. Zając, P. Drózdź, W. Janus, M. Szpytma, H. Nayyef, and T. Ślęzak, *APL Mater.* **8**, 061107 (2020).
- [27] S. Altieri, M. Finazzi, H. H. Hsieh, H. J. Lin, C. T. Chen, T. Hibma, S. Valeri, and G. A. Sawatzky, *Phys. Rev. Lett.* **91**, 137201 (2003).
- [28] D. Alders, L. H. Tjeng, F. C. Voogt, T. Hibma, G. A. Sawatzky, C. T. Chen, J. Vogel, M. Sacchi, and S. Iacobucci, *Phys. Rev. B* **57**, 11623 (1998).
- [29] A. Barra, A. Ross, O. Gomonay, L. Baldrati, A. Chavez, R. Lebrun, J. D. Schneider, P. Shirazi, Q. Wang, J. Sinova, G. P. Carman, and M. Kläui, *Appl. Phys. Lett.* **118**, 172408 (2021).
- [30] H. Qiu, L. Zhou, C. Zhang, J. Wu, Y. Tian, S. Cheng, S. Mi, H. Zhao, Q. Zhang, D. Wu, B. Jin, J. Chen, and P. Wu, *Nat. Phys.* **17**, 388 (2021).
- [31] J. Stöhr, A. Scholl, T. J. Regan, S. Anders, J. Lüning, M. R. Scheinfein, H. A. Padmore, and R. L. White, *Phys. Rev. Lett.* **83**, 1862 (1999).
- [32] F. Kronast and S. Valencia Molina, *J. Large-Scale Res. Facil. JLSRF* **2**, A90 (2016).
- [33] Y. S. Kiyotaka Nakahigashi, Nobuo Fukuoka, *J. Phys. Soc. Jpn.* **38**, 1634 (1975).
- [34] H. Gomonay and V. M. Loktev, *J. Phys.: Condens. Matter* **14**, 3959 (2002).
- [35] C. Teodosiu, *Elastic Models of Crystal Defects* (Springer, Berlin, 1982).
- [36] M. Kléman and M. Schlenker, *J. Appl. Phys.* **43**, 3184 (1972).
- [37] J. D. Eshelby, *Solid State Phys. Adv. Res. Appl.* **3**, 79 (1956).
- [38] C. Schmitt, L. Baldrati, L. Sanchez-Tejerina, F. Schreiber, A. Ross, M. Filianina, S. Ding, F. Fuhrmann, R. Ramos, F. Maccherozzi, D. Backes, M.-A. Mawass, F. Kronast, S. Valencia, E. Saitoh, G. Finocchio, and M. Kläui, *Phys. Rev. Appl.* **15**, 034047 (2021).
- [39] C. Kittel, *Rev. Mod. Phys.* **21**, 541 (1949).
- [40] J. A. Simmons, R. de Wit, and R. Bullough (Eds.), *Fundamental aspects of dislocation theory: conference proceedings, National Bureau of Standards, April 21-25, 1969*, Vol. 1 (US National Bureau of Standards, 1970).
- [41] K.-E. Kim, S. Jeong, K. Chu, J. H. Lee, G.-Y. Kim, F. Xue, T. Y. Koo, L.-Q. Chen, S.-Y. Choi, R. Ramesh, and C.-H. Yang, *Nat. Commun.* **9**, 403 (2018).
- [42] E. V. Gomonay and V. M. Lotkev, *Phys. Solid State* **47**, 1755 (2005).
- [43] R. White, R. Newt, and R. Pease, *IEEE Trans. Magn.* **33**, 990 (1997).
- [44] W. L. Roth and G. A. Slack, *J. Appl. Phys.* **31**, S352 (1960).
- [45] G. A. Slack, *J. Appl. Phys.* **31**, 1571 (1960).
- [46] O. Gomonay and D. Bossini, *J. Phys. D: Appl. Phys.* **54**, 374004 (2021).
- [47] R. de Wit, *J. Res. Natl. Bur. Stand., Sect. A* **77A**, 607 (1973).